RSC Advances

ROYAL SOCIETY OF CHEMISTRY

PAPER

View Article Online
View Journal | View Issue

Check for updates

Cite this: *RSC Adv.*, 2020, **10**, 42172

Synthesis of 2D $MoS_{2(1-x)}Se_{2x}$ semiconductor alloy by chemical vapor deposition†

Wenwen Yao,[ab] Zhilin Kang,[a] Jiajun Deng,[ab] Yan Chen,[ab] Qian Song,[a] Xun Lei Ding,[ab] Fangchao Lu[ab] and Wenjie Wang*[ab]

Received 10th September 2020
Accepted 6th November 2020

DOI: 10.1039/d0ra07776c

rsc.li/rsc-advances

Alloying/doping in two-dimensional (2D) materials is emerging as an increasingly important strategy due to the wide-range bandgap tunability and versatility of these materials. Monolayer 2D transition metal dichalcogenide (TMD) alloy has been investigated both theoretically and experimentally in recent years. Here, we synthesized a bilayer $MoS_{2(1-x)}Se_{2x}$ semiconductor alloy *via* the chemical-vapor deposition technique. The as-grown triangular $MoS_{2(1-x)}Se_{2x}$ flakes with size of roughly 10 μm were observed by optical microscope and scanning electron microscope (SEM). The 1.4–1.9 nm thickness of the samples, as measured by AFM, means that bilayer $MoS_{2(1-x)}Se_{2x}$ alloys were grown. The characteristic Raman modes related to Mo–S and Mo–Se vibrations were observed in the Raman spectrum. Two emission peaks were respectively found, corresponding to the A and B excitons in the photoluminescence (PL) spectrum. XPS measurements confirmed the Se doping of the alloy. The first-principles calculation results show a contraction of the band gap value with the increase of Se doping in the MoS_2 lattice. Compared with monolayer $MoS_{2(1-x)}Se_{2x}$ alloy, the band bending effect is more obvious, and the bilayer $MoS_{2(1-x)}Se_{2x}$ alloy still shows the direct band gap luminescence characteristic, which has certain guiding significance for the growth of two-dimensional materials and for device preparation.

Introduction

The transition-metal dichalcogenides have attracted intense attention due to their unique physical properties, and they have potential application as efficient electrodes in photoelectrochemical solar cells,[1–3] the catalyst industry, and in secondary batteries[4–6] or solid-state lubricants.[7] The typical transition-metal dichalcogenides MoS_2 and $MoSe_2$ have a structure composed of three similar sublayers: one layer of Mo atom sandwiched by two planes of S or Se atoms, and their bandgap variability is from 1.8 to 1.5 eV. Moreover, theoretical calculation and experimental work showed that the mixed layered crystals with thermodynamic stability allow continuous tuning of the band gap,[8] which enhances the application of the 2D transition-metal dichalcogenides in electronic and optoelectronic devices.[9,10] Among all kinds of approaches for tuning the bandgap, such as alloying/doping TMDs with other elements,[11] strain[12] or stacking in the form of heterostructures,[13] alloying/doping provides an easily scalable route to engineer the band structure.[14,15]

A variety of methods have been demonstrated in previous studies to synthesize monolayer $MoS_{2(1-x)}Se_{2x}$, including mechanical exfoliation of bulk material,[16] gentle sputtering,[17] physical vapor deposition,[18] and chemical vapor deposition.[19] Among these methods, the CVD technique is considered a promising method for the controllable synthesis of $MoS_{2(1-x)}Se_{2x}$ flakes, particularly for fabricating monolayer $MoS_{2(1-x)}Se_{2x}$. Also, theoretical (*ab initio*) calculations have been performed to reveal the modification of the band structure and bandgap of monolayer MoS_2 with Se doping.[20] In order to explore the bandgap difference between bilayer and monolayer $MoS_{2(1-x)}Se_{2x}$, the $MoS_{2(1-x)}Se_{2x}$ flakes were synthesized by the low-pressure chemical vapor deposition technique. The difficulty in synthesizing $MoS_{2(1-x)}Se_{2x}$ bilayer is in controlling the growth parameters in the alloying process, such as deposition temperature, evaporation concentration, and pressure for deposition. The bilayer $MoS_{2(1-x)}Se_{2x}$ alloys are found to be achieved easily when x is smaller than 50% in Ar atmosphere.

Experiments

In the present work, MoS_2 bilayer and $MoSe_2$ bilayer with controllable morphology and size were firstly obtained using chemical vapor deposition (CVD), and the optical bandgaps of the resulting compounds are 1.53 and 1.82 eV, as given by photoluminescence spectra. Then, we explore the bandgap of $MoS_{2(1-x)}Se_{2x}$ bilayer as a function of Se/S ratio. The growth of

---

[a] *School of Mathematics and Physics, North China Electric Power University, Beijing 102206, China. E-mail: wwj2008@ncedu.edu.cn*

[b] *Institute of Clusters and Low Dimensionals, North China Electric Power University, Beijing 102206, China*

† Electronic supplementary information (ESI) available. See DOI: 10.1039/d0ra07776c

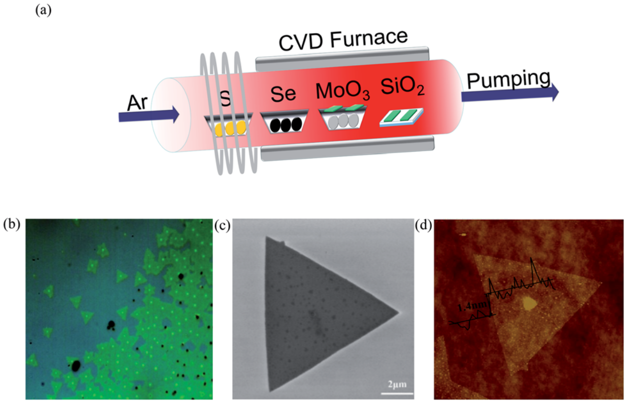

Fig. 1 (a) Illustration of the three-heating-zone furnace setup for $MoS_{2(1-x)}Se_{2x}$ growth; (b) OM image, (c) SEM image and (d) AFM image of bilayer $MoS_{2(1-0.37)}Se_{2(0.37)}$.

$MoS_{2(1-x)}Se_{2x}$ sheets was carried out in a three-zone tube furnace with a 2.5-inch diameter quartz tube, as shown in Fig. 1(a), where different shades of red indicate different temperatures. Sulfur, selenium and molybdenum trioxide precursors were loaded in ceramic boats and were placed from downstream to upstream in the furnace tube, respectively. Argon gas of 200 sccm was provided throughout the experiment. The furnace was heated to 650 °C at a rate of 10 °C min^{-1}; in the meantime, selenium was heated to 350 °C and sulfur was heated to 250 °C by heating belt. When the furnace reached 850 °C, the argon gas carries the vaporized selenium, sulfur and molybdenum trioxide to the substrates during the deposition process. After the growth, the furnace was naturally cooled to room temperature. The heating and cooling process of the tube furnace in the experiment is shown in Fig. S1.† More details of the experiment can be seen in the ESI.†

Results and discussion

A typical optical image of the as-grown bilayer $MoS_{2(1-0.37)}Se_{2(0.37)}$ is shown in Fig. 1(b). It is not difficult to find some dots distributed within the surface of the $MoS_{2(1-x)}Se_{2x}$ samples. The bright dot located at the center of the nanoflake indicates the original nucleation sites for the crystals. Similar to the perylene-3,4,9,10-tetracarboxylic acid tetrapotassium salt (PTAS) of MoS_2,[21] we can conclude that these bright dots coming from PTAS serve as a seeding promoter for the growth of the $MoS_{2(1-x)}Se_{2x}$. The shape and scale of $MoS_{2(1-0.37)}Se_{2(0.37)}$ are given by the SEM images shown in Fig. 1(b). Unlike $SbTe_2$,[22] α-MoO_3 (ref. 23) and Bi_2Se_3,[24] MoS_2 (ref. 25) and $MoSe_2$ (ref. 26) grow in the triangular direction. By controlling the quantity of evaporation source, triangles of $MoS_{2(1-x)}Se_{2x}$ with a size >5 μm were obtained. It is noteworthy that the morphology of the material will not be influenced by the composition. As displayed in Fig. 1(c), the thickness and morphology of $MoS_{2(1-0.37)}Se_{2(0.37)}$ was further confirmed by AFM technique. The height profile from the Si/SiO_2 substrate to the triangular regions falls in the range of 1.4 nm, which is in good relation to the thickness of the $MoS_{2(1-0.37)}Se_{2(0.37)}$ bilayer.

Raman spectroscopy (wavelength of laser, 514 nm) was used to investigate the structure of the $MoS_{2(1-x)}Se_{2x}$ samples. Two sets of Raman peaks are observed in Fig. 2(a). One set of Raman peaks are MoS_2-like peaks around 380–400 cm^{-1}, which can be attributed to the E1 2g mode resulting from in-plane vibration and the A_{1g} mode originating from out-of-plane vibration.[27] Also, the intensity of A_{1g} mode is higher than that of E1 2g mode because the intralayer bonding is thought to be strong and predominantly covalent, whereas the interlayer weak bonding is of the van der Waals type.[28] The other set, consisting of 240 and 280 cm^{-1} peaks, corresponds to $MoSe_2$-like A_{1g} and E1 2g modes, but slightly shifts to lower wavenumber values than those of pure $MoSe_2$.[29] Apart from these peaks, the spectrum contains a peak around 300 cm^{-1}, which is independent of the composition.[30] It is reasonable to infer that the peak is ascribed to the silicon substrate. It should be noted that the original material MoS_2 bilayer has two Raman modes, as earlier reported, and by introducing the Se during the growth process, the synthesized $MoS_{2(1-x)}Se_{2x}$ alloy presents two sets of Raman modes. Moreover, with the increasing Se component, the intensity of MoS_2-like modes weakens gradually and finally disappears, but the intensity of $MoSe_2$-like modes is enhanced, which agrees with the reported result of monolayer material.[31] In addition, the kind and intensity of Raman peaks were changed with the introduction of Se to the original MoS_2, as shown in Fig. 2(c). All peaks are shifted to lower wavenumbers with increasing Se content, which is consistent with the behavior of monolayer $MoS_{2(1-x)}Se_{2x}$.[32] The pristine monolayer MoS_2 consists of three sublayers, one layer of Mo atom sandwiched by two planes of sulfur atoms. As the Se atoms substitute for a part of the S sites, the symmetry of original MoS_2 crystals is broken due to the larger radius of Se atoms.[33] The original Mo–S and Mo–Mo bond lengths are changed by the distortion, leading to an external tensile stress exerting on the original MoS_2 lattice. Therefore, the atomic vibration due to the E1 2g and A_{1g} modes of MoS_2 is softened.[34]

Photoluminescence measurements were performed to study the optical properties of as-grown $MoS_{2(1-x)}Se_{2x}$. We control the composition of the alloy by adjusting the amount of reactants Se, S and MoO_3. The photoluminescence spectra of the bilayer $MoS_{2(1-x)}Se_{2x}$ (x = 0–1) are shown in Fig. 2(b). In comparison with monolayer $MoS_{2(1-x)}Se_{2x}$, all bilayer alloys have two PL peaks originating from the direct excitonic transition at the K-point of the first Brillouin zone.[35] The peak located at the higher wavelength is generally termed as exciton A, and the other at the lower wavelength as exciton B.[36] The difference between these PL peaks can be inferred from the spin–orbit coupling of the valence band.[37] The plots of A and B exciton energy of bilayer $MoS_{2(1-x)}Se_{2x}$ with different Se contents (x) are displayed in Fig. 2(d). The results reveal that the emission energy can be continually tuned from 1.82 eV (680 nm) to 1.53 eV (810 nm). We find a decrease of the optical bandgap with Se content increasing in the bilayer $MoS_{2(1-x)}Se_{2x}$ alloy, which is similar to monolayer $MoS_{2(1-x)}Se_{2x}$. However, the bandgap bowing effect is more obvious than that in monolayer $MoS_{2(1-x)}Se_{2x}$.[38] There is no doubt that the redshift of PL peaks is related to the band structure variation *via* Se introduction to MoS_2. According to the

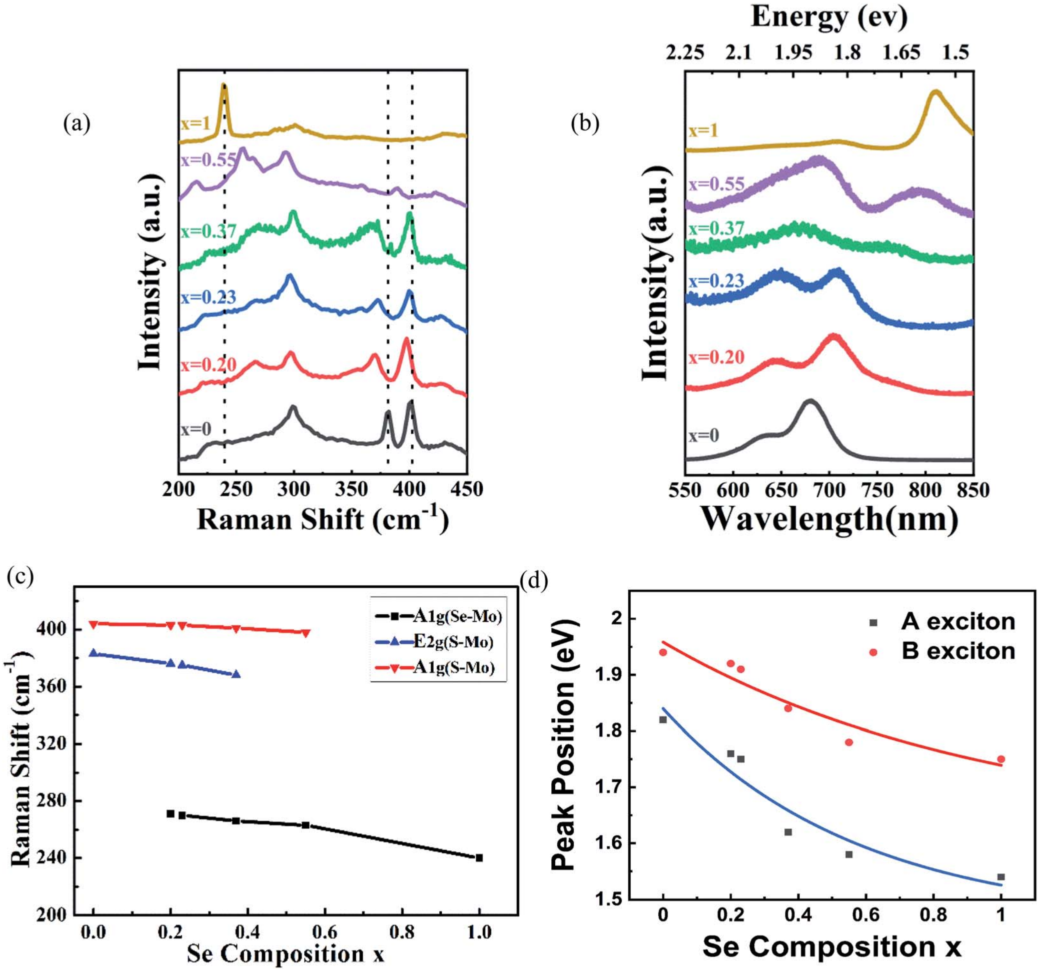

Fig. 2 (a) Raman spectra and (b) PL spectra of the bilayer $MoS_{2(1-x)}Se_{2x}$ ($x = 0.00$–1.00); (c) plots of $MoS_{2(1-x)}Se_{2x}$ Raman modes with Se composition increasing; (d) plots of A-exciton and B-exciton energy of $MoS_{2(1-x)}Se_{2x}$.

molecular orbital theory, the non-bonding d bands of MoS_2 are mainly derived from the Mo-d_{z^2}, Mo-$d_{x^2-y^2,xy}$ and Mo-$d_{xz,yz}$ orbitals.[39,40] Mo and S atoms are coordinated through ionic–covalent interaction. With Se introduction into MoS_2, the strong covalent effects in $MoS_{2(1-x)}Se_{2x}$ subsequently occur, resulting in the non-bonding d bands broadening and, thus, the band gap reduced.[28,39] Beyond the optical properties based on PL, we evaluated the stoichiometric features of bilayer $MoS_{2(1-x)}Se_{2x}$.

According to the following formula, a quadratic rule is introduced to describe the relationship between bandgap and x value of the ternary alloy:

$$E_g(x) = xE_g(MoSe_2) + (1 - x)E_g(MoS_2) - bx(1 - x), \quad (1)$$

where $E_g(x)$ is the bandgap of the alloy. We can firstly estimate the x of as-grown $MoS_{2(1-x)}Se_{2x}$. In bilayer $MoS_{2(1-x)}Se_{2x}$, we choose B exciton energy in the PL spectrum as $E_g(x)$, and b is the bowing parameter of $MoS_{2(1-x)}Se_{2x}$, approximated to 0.05.[41] The calculated x values are approximately equal to 0.20, 0.22, 0.41 and 0.50. On the other hand, X-ray photoelectron spectroscopy (XPS) was adapted to characterize the chemical composition of crystals. In Fig. 3, the XPS spectrum of as-grown $MoS_{2(1-0.37)}Se_{2(0.37)}$ is displayed. The Mo 3d, S 2p, and Se 3d regions of the XPS spectra for $MoS_{2(1-0.37)}Se_{2(0.37)}$ with different Se composition can be deconvoluted into various peaks. The Mo 3d window (Fig. 3(a)) consists of Mo^{4+} 3d5/2, Mo^{4+} 3d3/2, Mo^{6+} and S 2s, and the corresponding binding energies are 229.5, 232.6, 235.7 and 226.8 eV, which is in good agreement with the previous literature.[42] The presence of Mo^{4+} 3d5/2, Mo^{4+} 3d3/2 and S 2s is due to Mo 3d spin–orbit splitting in the formation of MoS_2 and $MoSe_2$. The reason for Mo^{6+} in the energy spectrum may be the presence of $MoO_{3-x}S_x$ in the reaction system. $MoO_{3-x}S_x$ may be derived from incomplete vulcanization (or selenization) of metal Mo during the heating process, or it may be generated by the partial decomposition of $MoS_{2(1-x)}Se_{2x}$ deposited during the cooling process. The S 2p doublet is shown in Fig. 3(b), and it exhibits two peaks located at 162.4 eV and 163.6 eV, corresponding to S 2p3/2 and S 2p1/2 components, respectively. Further, as displayed in Fig. 3(c), the Se 3d spectra can be deconvoluted into two peaks at 54.9 eV and 55.7 eV, corresponding to Se 3d3/2 and Se 3d5/2 components, respectively. The orbital binding energy diagram of S 2p and Se 3d with doping concentration is shown in Fig. S2.† From the XPS results, we analyze the Se/S ratio by eqn (2),[37]

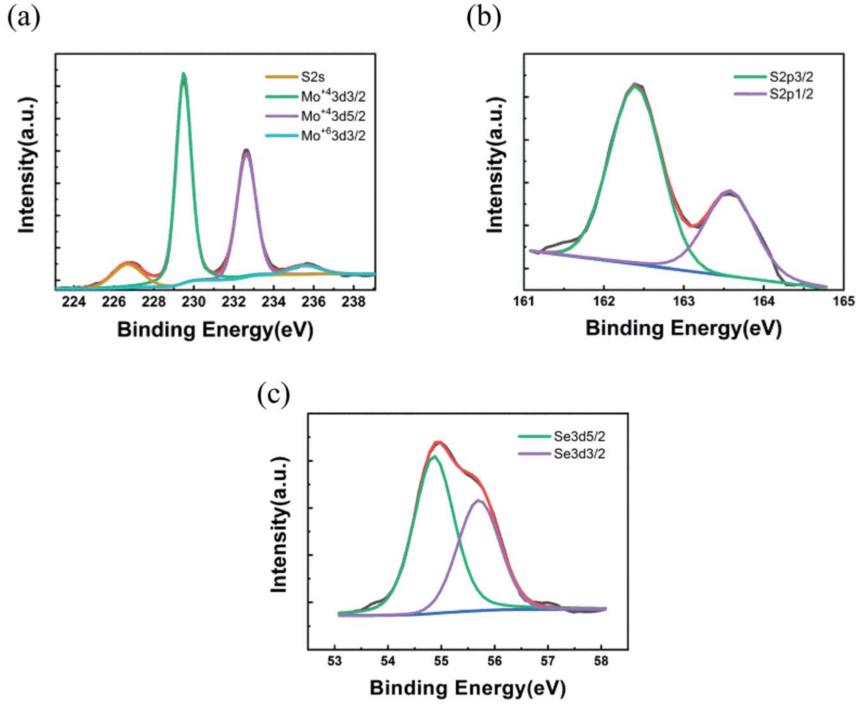

Fig. 3 XPS spectra of $MoS_{2(1-0.37)}Se_{2(0.37)}$: (a) Mo 3d; (b) S 2p; (c) Se 3d.

$$\frac{\mathrm{Se}}{\mathrm{S}} = \frac{(I_{\mathrm{Se}} \times F_{\mathrm{S}})}{(I_{\mathrm{S}} \times F_{\mathrm{Se}})} \tag{2}$$

where the F_S and F_{Se} are the relative sensitivity factors for S 2p3/2 (0.4453) and Se 3d3/2 (0.8493);[43] I_S and I_{Se} represent the areas of the S and Se peaks. The Se content x was estimated to be 0.20, 0.23, 0.37 and 0.55, corresponding to the Se/S ratios of 0.40 : 1.60, 0.46 : 1.54, 0.74 : 1.26 and 1.10 : 0.90, respectively. As compared with the x value obtained from the bandgap (B exciton) by formula (1), the XPS results are in good agreement with the theoretically calculated value, as displayed in Fig. 4. The good agreement also indicates that the B exciton energy can be used to estimate the bandgap of bilayer $MoS_{2(1-x)}Se_{2x}$.

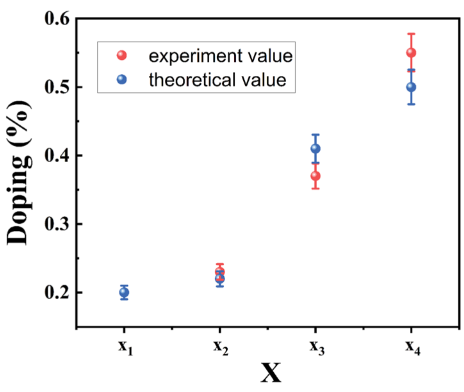

Fig. 4 Se composition of as-grown $MoS_{2(1-x)}Se_{2x}$ by two methods.

In order to further understand the properties of bilayer $MoS_{2(1-x)}Se_{2x}$ semiconductor alloy with different Se doping concentrations, we chose VASP (Vienna *ab initio* simulation package) for density functional theory (DFT) calculation and used the Perdew–Burke–Ernzerhof (PBE) functional to evaluate the band gap changes of the doped alloys.[44] The 4 × 4 × 2 supercell was selected for the study of the pristine bilayer MoS_2, which contains 96 atoms (32 Mo atoms and 64 S atoms). The side and top views of the atomic structure of $MoS_{2(1-0.37)}Se_{2(0.37)}$ are shown in Fig. 5(a) and (b), respectively. MO, Se and S are represented by purple, green and yellow, respectively. The results of DFT calculation show that the bilayer MoS_2 is an indirect band gap semiconductor with a band gap value of 1.70 eV, as seen in Fig. 5(c), which is consistent with a previous report.[45] The direct bandgap of bilayer $MoSe_2$ is 1.42 eV, which is lower than the 0.28 eV of bilayer MoS_2. The band structures calculated at $x = 0$, 0.20, 0.37, 0.55 and 1 are shown in Fig. 5(d), and with the increase of Se doping content, the band gap value of bilayer $MoS_{2(1-x)}Se_{2x}$ alloy has a decreasing trend corresponding to the PL spectrum shown in Fig. 2(b), but the band gap values are slightly lower than the experimental values. From the band structure theory, when Se enters the MoS_2 lattice, the highest occupied molecular orbital (HOMO) and lowest unoccupied molecular orbital (LUMO) approach the Fermi level, resulting in band gap value decrease, which is a contraction of the band gap value.[39] Compared with monolayer $MoS_{2(1-x)}Se_{2x}$ alloy, the band bending effect of bilayer $MoS_{2(1-x)}Se_{2x}$ alloy is more obvious,[46] and the bilayer $MoS_{2(1-x)}Se_{2x}$ alloy still shows the luminescence characteristic of direct band gap, which benefits the electronic structure research of 2D materials.

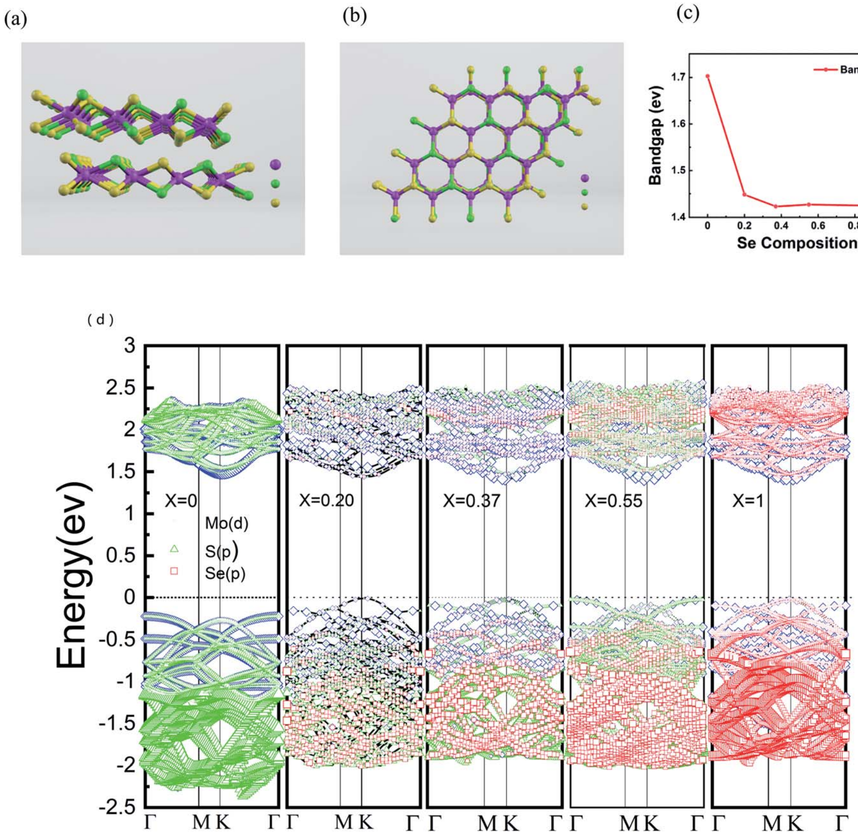

Fig. 5 (a and b) Side view and top view of the atomic structure of $MoS_{2(1-0.37)}Se_{2(0.37)}$. MO, Se and S are represented by purple, green and yellow atoms, respectively. (c) Band energy of $MoS_{2(1-x)}Se_{2x}$ when $x = 0$, 0.20, 0.37, 0.55, 1; (d) electronic band structure of bilayer Se-doped MoS_2.

Conclusion

We have demonstrated an approach for preparing bilayer MoS_2 using low-pressure chemical vapor deposition. Then, by introducing the Se component in the growth process of MoS_2, $MoS_{2(1-x)}Se_{2x}$ bilayers with various Se contents were synthesized. The formation of triangular-shaped microcrystals was confirmed by SEM, AFM, Raman, PL and XPS measurements. Because the MoS_2 lattice is modified by Se doping, the grown alloys possess bandgaps between the values characteristic of bilayer MoS_2 and $MoSe_2$. The two sets of Raman modes and two PL peaks of bilayer $MoS_{2(1-x)}Se_{2x}$ are consistent with the variation trend of the properties of monolayer $MoS_{2(1-x)}Se_{2x}$. Furthermore, we regard the B exciton energy as the bandgap of $MoS_{2(1-x)}Se_{2x}$ ranging from 1.82 eV to 1.53 eV to estimate the x values, which is in good agreement with the XPS result. Additionally, we also use first-principles calculations to confirm the experimental results. With the addition of Se to bilayer MoS_2 lattice, the band gap decreases. Changing of the Se/S ratio in growth crystals results in the band structure and bandgap adjustment, which provides a promising approach to produce 2D crystals with fancy properties in particular applications. The application of layered $MoS_{2(1-x)}Se_{2x}$ could be further considered in later papers.

Conflicts of interest

There are no conflicts to declare.

Acknowledgements

This work was supported by the Fundamental Research Funds for the Central Universities (JB2019MS051, JB2015RCY03, JB2020MS042) and the National Natural Science Foundation of China (No. 91545122, No. 61704054).

References

1 E. Fortin and F. Raga, *Phys. Rev. B: Condens. Matter Mater. Phys.*, 1975, **11**, 905.
2 W. Kautek, H. Gerischer and H. Tributsch, *Cheminform*, 1981, **12**, 2471.
3 K. K. Kam and B. A. Parkinson, *J. Phys. Chem. C*, 1982, **86**, 463.
4 S. J. Li, J. C. Bernède, J. Pouzet and M. Jamali, *J. Phys. Condens. Matter*, 1996, **8**, 2291.
5 P. G. Moses, B. Hinnemann, H. Topsøe and J. K. Nørskov, *J. Catal.*, 2007, **248**, 188.
6 P. Grange and B. Delmon, *J. Less Common Met.*, 1974, **36**, 353.
7 C. T. Tye and K. J. Smith, *Catal. Today*, 2006, **116**, 461.

8 Y. J. Wu, P. H. Wu, J. Jadczak, Y. S. Huang, C. H. Ho, H. P. Hsu and K. K. Tiong, *J. Appl. Phys.*, 2014, **115**, 193.

9 Y. Yoon, K. Ganapathi and S. Salahuddin, *Nano Lett.*, 2011, **11**, 3768.

10 J. Liu, Z. Zeng, X. Cao, G. Lu, L. H. Wang, Q. L. Fan, W. Huang and H. Zhang, *Small*, 2012, **8**, 3517.

11 A. A. Tedstone, D. J. Lewis and P. O'Brien, *Chem. Mater.*, 2016, **28**, 1965.

12 P. Johari and V. B. Shenoy, *ACS Nano*, 2012, **6**, 5449.

13 X. Hu, L. Kou and L. Sun, *Sci. Rep.*, 2016, **6**, 31122.

14 Z. m. Shi, Z. h. Zhang, A. Kutana and B. I. Yakobson, *ACS Nano*, 2015, **9**, 9802.

15 Q. Zeng, H. Wang, W. Fu, Y. Gong and Z. Liu, *Small*, 2015, **11**, 1868.

16 K. Zhou, N. Mao, H. Wang, Y. Peng and H. Zhang, *Angew. Chem., Int. Ed.*, 2011, **50**, 10839.

17 Q. Ma, M. Isarraraz, C. S. Wang, E. Preciado, V. Klee, S. Bobek, K. Yamaguchi, E. Li, P. M. Odenthal, N. Ariana, D. Barroso, D. Sun, G. v. S. Palacio, M. Gomez, N. Andrew, D. Le, G. Pawin, J. Mann, T. F. Heinz, T. S. Rahman and L. Bartels, *ACS Nano*, 2014, **8**, 4672.

18 Q. Feng, N. Mao, J. Wu, H. Xu and L. Xie, *ACS Nano*, 2015, **9**, 7450.

19 L. Yang, Q. Fu, W. Wang, J. Huang, J. Huang, J. Zhang and B. Xiang, *Nanoscale*, 2015, **7**, 10490.

20 G. Li, M. Q. Chen, S. X. Zhao, P. W. Li, J. Hu, S. B. Sang and J. J. Hou, *Acta Phys.-Chim. Sin.*, 2016, **32**, 2905.

21 X. Ling, Y. H. Lee, Y. Lin, W. Fang and J. Kong, *Nano Lett.*, 2014, **14**, 464.

22 K. A. Kokh, V. V. Atuchin, T. A. Gavrilova, N. V. Kuratieva, N. V. Pervukhina and J. S. S. C. Surovtsev, *Solid State Commun.*, 2014, **177**, 16.

23 V. V. Atuchin, T. A. Gavrilova, T. I. Grigorieva, N. V. Kuratieva, K. A. Okotrub, N. V. Pervukhina and N. V. Surovtsev, *J. Cryst. Growth*, 2011, **318**, 987.

24 V. V. Atuchin, S. V. Borisov, T. A. Gavrilova, K. A. Kokh, N. V. Kuratieva and N. V. Pervukhina, *Particuology*, 2016, **26**, 118.

25 J. Chen, W. Tang, B. Tian, B. Liu, X. Zhao, Y. Liu, T. Ren, W. Liu, D. Geng, H. Y. Jeong, H. S. Shin, W. Zhou and K. P. Loh, *Adv. Sci.*, 2016, **3**, 1600033.

26 J. Xia, X. Huang, L.-Z. Liu, M. Wang, L. Wang, B. Huang, D.-D. Zhu, J.-J. Li, C.-Z. Gu and X.-M. Meng, *Nanoscale*, 2014, **6**, 8949.

27 H. S. S. R. Matte, A. Gomathi, A. K. Manna, D. J. Late and R. Datta, *Angew. Chem., Int. Ed.*, 2010, **49**, 4059.

28 A. R. Beal and H. P. Hughes, *J. Phys. C Solid State Phys.*, 1979, 881.

29 H. Tang, K. Dou, C. C. Kaun, Q. Kuang and S. Yang, *J. Mater. Chem. A*, 2013, **2**, 360.

30 S. G. Pandya and M. E. Kordesch, *Nanoscale Res. Lett.*, 2015, **10**, 1.

31 Q. Gong, L. Cheng, C. Liu, M. Zhang and Y. Li, *ACS Catal.*, 2015, **5**, 2213.

32 H. Li, X. Duan, X. Wu, X. Zhuang, H. Zhou, Q. Zhang, X. Zhu, W. Hu, P. Ren and P. Guo, *J. Am. Chem. Soc.*, 2014, **136**, 3756.

33 S. Horzum, H. Sahin, S. Cahangirov, P. Cudazzo, A. Rubio, T. Serin and F. M. Peelers, *Phys. Rev. B: Condens. Matter Mater. Phys.*, 2013, **87**, 125415.

34 A. Castellanos-Gomez, R. Roldán, E. Cappelluti, M. Buscema, F. Guinea, d. Z. Van, S. J. Herre and G. A. Steele, *Nano Lett.*, 2013, **13**, 5361.

35 G. Eda, H. Yamaguchi, D. Voiry, T. Fujita and M. Chen, *Nano Lett.*, 2011, **12**, 1.

36 K. F. Mak, C. Lee, J. Hone, J. Shan and T. F. Heinz, *Phys. Rev. Lett.*, 2010, **105**, 136805.

37 V. Kiran, D. Mukherjee, R. N. Jenjeti and S. J. N. Sampath, *Nanoscale*, 2014, **6**, 12856.

38 Q. Feng, Y. Zhu, J. Hong, M. Zhang, W. Duan, N. Mao, J. Wu, H. Xu, F. Dong and F. Lin, *Adv. Mater.*, 2014, **26**, 2763.

39 B. Rajbanshi, S. Sarkar and P. Sarkar, *Phys. Chem. Chem. Phys.*, 2015, **17**, 26166.

40 M. Chhowalla, H. S. Shin, G. Eda, L. J. Li, K. P. Loh and H. Zhang, *Nat. Chem.*, 2013, **5**, 263.

41 J. A. Wilson and A. D. Yoffe, *Adv. Phys.*, 1969, **18**, 193.

42 J. Kang, S. Tongay, J. Li and J. Wu, *J. Appl. Phys.*, 2013, **113**, 10451.

43 S. Umrao, J. Jeon, S. M. Jeon, Y. J. Choi and S. Lee, *Nanoscale*, 2017, **9**, 594.

44 W. Zhang, X. Li, T. Jiang, J. Song, Y. Lin, L. Zhu and X. Xu, *Nanoscale*, 2015, **7**, 13554.

45 S. Andrea, L. Sun, Y. Zhang, T. Li and J. Kim, *Nano Lett.*, 2010, **10**, 1271.

46 Q. Feng, Y. Zhu, J. Hong, M. Zhang, W. Duan, N. Mao, J. Wu, H. Xu, F. Dong and F. Lin, *Adv. Mater.*, 2014, **26**, 2763.